Journal of Materials Research and Technology 33 (2024) 8321–8328

Contents lists available at ScienceDirect

Journal of Materials Research and Technology

journal homepage: www.elsevier.com/locate/jmrt

Influence of liquid metal embrittlement on the failure behavior of dissimilar spot welds with advanced high-strength steel: A component study

Keke Yang [a,*], Matthias Sowada [a], Viktoria Olfert [a], Georg Seitz [b], Vincent Schreiber [c], Marcel Heitmann [a], David Hein [a], Max Biegler [b], Sven Jüttner [c], Michael Rethmeier [e,d,b], Gerson Meschut [a]

[a] Laboratory for Material and Joining Technology (LWF), Paderborn University, 33098, Paderborn, Germany
[b] Fraunhofer Institute for Production Systems and Design Technology (IPK), 10587, Berlin, Germany
[c] Institute of Materials and Joining Technology (IWF), Otto-von-Guericke University Magdeburg, 39106, Magdeburg, Germany
[d] Federal Institute for Materials Research and Testing (BAM), 12205, Berlin, Germany
[e] Institute for Machine Tools and Factory Management (IWF), Technical University of Berlin, 10623, Berlin, Germany

ARTICLE INFO

Handling editor: L Murr

Keywords:
Liquid metal embrittlement
Resistance spot welding
Impact loading
Crack propagation
Advanced high-strength steel

ABSTRACT

This study investigates the effects of liquid metal embrittlement (LME) cracks on the mechanical performance of resistance spot-welded joints in zinc-coated advanced high-strength steel (AHSS) at the component level. To this end, a novel component-level test specimen featuring a hat and L-shaped profile was developed to identify critical failure points under three-point bending loads. Load-bearing capacity tests were subsequently conducted under both quasi-static and impact loading conditions, specifically targeting LME cracks with an average depth reaching 63.6% of the sheet thickness. By monitoring the surface strain of spot welds affected by LME cracks, the study visualizes stress concentration effects at the crack tips and traces the propagation of these cracks into the base material, which ultimately leads to material tearing and joint failure. The findings reveal that the effect of LME cracks in reducing load-bearing capacity is more pronounced under impact loading than under quasi-static loading, highlighting a previously underexplored aspect of LME behavior under impact loading. Specifically, the peak load decreased by 3.9% and 10.8%, while energy absorption declined by 52.2% and 78.3% under quasi-static and impact loading, respectively.

1. Introduction

Automobile manufacturers emphasize lightweight designs to improve driving safety while reducing emissions [1]. Advanced High-Strength Steels (AHSS) are highly regarded for their optimal combination of elongation and tensile strength, effectively fulfilling these objectives [2]. For anti-corrosion purposes, these steels are protected with zinc-based coatings [3]. As a primary joining technique in automotive body manufacturing, resistance spot welding (RSW) is commonly used to join these steels [4]. However, there is a significant risk of liquid metal embrittlement (LME) during the RSW of zinc-coated AHSS [5]. The combination of tensile stresses caused by electrode indentation during RSW permits molten zinc to penetrate the grain boundaries of AHSS, thereby weakening the material and resulting in LME-induced crack-like fractures [6]. According to Ref. [7], LME cracks can be categorized into four types based on their location, as shown in Fig. 1. The cracks on the spot weld surface include: (i) cracks located beneath the electrode surface (Type A); (ii) those at the indentation shoulder (Type B); (iii) those in the heat-affected zone (HAZ) (Type C); and (iv) cracks at the interface between the sheets near the notch tip (Type D).

Although strategies such as employing larger working plane electrode caps [8] and extending hold times [9] have been proposed to prevent LME cracks, the former is highly sensitive to electrode misalignment, while the latter extends the welding cycle time. These limitations restrict the practical application of these approaches. Moreover, LME is an inherently complex phenomenon, influenced not only by the steel type but also by surface conditions [10], parameters of the galvanizing process [11], temperature and strain rate during loading [12], and grain boundary characteristics [13]. Furthermore, the welding conditions and the resulting thermo-mechanical gradients within the weld zone are critical to LME occurrence [14]. This complexity

* Corresponding author.
E-mail address: keke.yang@lwf.uni-paderborn.de (K. Yang).

https://doi.org/10.1016/j.jmrt.2024.11.166
Received 10 October 2024; Received in revised form 17 November 2024; Accepted 17 November 2024
Available online 19 November 2024

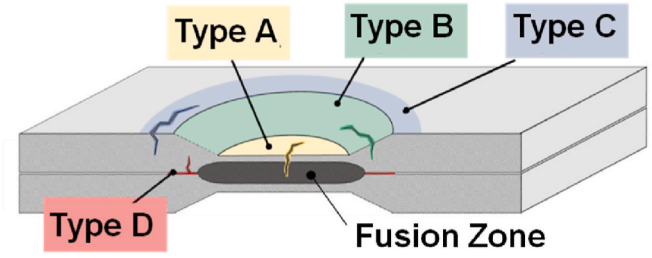

Fig. 1. Categories of LME cracks according to Ref. [7].

frequently leads to cases where a particular steel grade may appear resistant to LME under specific conditions but becomes vulnerable in different circumstances [15]. Hence, understanding the influence of LME cracks on the load-bearing capacity of joints is vital for the advancement of AHSS applications.

Consequently, numerous studies have explored the effect of LME cracks on the mechanical behavior of RSW joints. Gaul et al. [16] examined 1.5 mm thick CP800 and TRIP700 steel sheets, classifying the detected cracks as Type C. Their research, conducted under cyclic tensile shear loading, demonstrated that cracks with depths not exceeding 43% of the sheet thickness did not significantly impact fatigue life or structural stiffness. In a separate study, Benlatreche et al. [17] analyzed AHSS800, AHSS1050, and AHSS1180 steels, with thicknesses ranging from 1.0 mm to 1.4 mm. They identified Type A and Type C cracks, which extended nearly through the full sheet thickness, as detrimental to material strength and head tensile load-bearing capacity, leading to a 30% reduction in tensile shear strength, a 20% decrease in head tensile strength, and an 8% decline in fatigue life under cyclic loading. Similarly, Choi et al. [18] investigated TRIP1180 steel (1.6 mm) and reported a 40% reduction in head tensile strength and energy absorption capacity when cracks reached 40% of the sheet thickness under cyclic and quasi-static tensile shear loading. Furthermore, DiGiovanni et al. [19] assessed TRIP690 and DP980 steels, both with a thickness of 1.2 mm, and observed reductions in tensile shear strength of 2.6% and 7.1%, respectively, compared to zinc-removed materials. They also reported a substantial 43.5% decrease in tensile shear strength when crack depth reached 68% in TRIP1100 steel. In a subsequent study, DiGiovanni et al. [20] demonstrated that Type A and Type C cracks in TRIP1100 steel (1.6 mm) resulted in crack depths of 31%, with cracks along the primary load-bearing path causing a reduction in tensile shear strength by up to 30%. The findings emphasize that crack location is critical within the primary load-bearing path.

The aforementioned studies have substantially advanced the understanding of the effects of LME cracks on the mechanical behavior of RSW joints. However, the majority of existing studies remain focused on LME behavior under quasi-static and fatigue loads, with experimental samples predominantly consisting of laboratory-standard flat specimens. Research focusing on component-level specimens, particularly under impact loading conditions, remains scarce. Addressing this gap is crucial for understanding the influence of LME cracks on spot weld behavior, as the significantly increased strain rate under impact loading [21] may alter the extent to which LME cracks contribute to joint failure. Biro's 2023 review of current LME research [22] further underscores the importance of addressing this limitation.

To address these limitations, this study investigates the influence of LME cracks on the mechanical behavior of RSW joints in 3rd generation AHSS, utilizing component-level test specimens. After characterizing the formation of LME cracks, the load-bearing capacity was first assessed under quasi-static three-point bending conditions, employing an optical measurement system to measure joint surface deformation. Subsequently, the same test was conducted under impact loading using a sled test rig, with high-speed cameras capturing the entire failure process. The use of optical measurement systems facilitated the investigation of the impact of LME cracks on the mechanical performance of RSW joints, providing a deeper understanding of their failure mechanisms.

2. Research question and novelty

While previous studies, as reviewed earlier, have examined the impact of LME cracks on the load-bearing capacity of joints under quasi-static and cyclic loading conditions, the influence of LME cracks under impact loading—a factor critical to vehicle safety— has not been sufficiently studied. Furthermore, existing research mainly uses single-joint flat specimens in laboratory conditions, with limited systematic analysis of component-level specimens featuring multiple joints. These constraints restrict the direct applicability of current findings to full-scale vehicle applications.

To bridge these gaps, this study adopts a novel perspective by employing specially designed component-level test specimens with multiple joints, systematically investigating the impact of in-situ LME cracks (hereafter referred to as "LME cracks") on the load-bearing capacity of RSW joints. To this end, the research introduces an innovative component-level specimen design and experimental configuration, focusing on the mechanical behavior of joints with LME cracks under impact loading conditions. This comprehensive investigation advances understanding in the research field and supports the effective application of laboratory findings to component-level engineering scenarios.

3. Experimental setup and details

3.1. Resistance spot welding

In the experimental setup, RSW was conducted using a pedestal servo-electric *C*-type welding gun operating with a 1 kHz medium-frequency direct current. To maintain proper electrode temperature, water cooling was applied at a flow rate of 4 L/min as recommended in Ref. [23]. The electrode caps used conformed to the F1-16-20-50-5.5 specifications outlined in Ref. [24]. The selection of welding parameters was based on the guidelines in Ref. [25], as shown in Table 1. The chosen current intensity represented the maximum expulsion-free welding current. In this study, the welding time was doubled to induce severe LME cracks, representing a worst-case scenario for analysis. These non-standard welding conditions have been outlined in Refs. [26,27].

3.2. Materials and methods

The experiments use a 3rd generation AHSS, specifically a high-ductility dual-phase (DP) steel classified as DP1200 DH, which also corresponds to the CR850Y1180T-DH designation as outlined in Ref. [28]. Both surfaces of the steel were electrogalvanized (EG) with a minimum coating weight of 53 g/m^2. In this study, DP1200 DH was paired with a hot-dip galvanized (HDG) mild steel (DX56D), which also corresponds to the CR4 designation as outlined in Ref. [28]. The chemical compositions and mechanical properties of these materials are detailed in Tables 2 and 3, respectively. Furthermore, the selection of this material and thickness combination was driven by current industrial needs [29]. In the experimental setup, the DP1200 DH was positioned as the upper sheet on the anode side, while the DX56D acted as the lower sheet on the cathode side.

In order to create a control group without LME cracks, the zinc coating was removed before RSW using a 20% hydrochloric acid

Table 1
Welding parameters.

Electrode force in kN	Squeeze time in ms	Welding time in ms	Welding current in kA	Holding time in ms
4.5	300	760	9.5	300

Table 2
Chemical composition of the utilized material combination (expressed in weight– %).

	C	Si	Mn	P	Al	Ti	B	Cu
DP1200 DH	0.23	2.00	2.9	0.05	0.015–2.0	0.15	0.005	0.2
DX56D	0.12	0.50	0.6	0.10	–	0.30	–	–

Table 3
Mechanical properties of the utilized material combination determined by tensile test.

	Thickness in mm	0.2% Yield Strength $R_{p0.2}$ in MPa	Tensile Strength R_m min. in MPa	Total elongation A80 min in %
DP1200 DH	1.51	922	1247	13
DX56D	2.00	120–180	260–350	39

solution. Additionally, to enhance crack visibility after RSW, the zinc coating was removed using the same solution. To facilitate further analysis and quantify the depth of LME cracks, cross-sectional samples of the spot welds were prepared for metallographic examination. The samples were first etched with a 4% nital solution to evaluate the microstructures and measure the LME crack depth under an optical microscope. Subsequently, scanning electron microscope (SEM) analysis was conducted to characterize the crack morphology. Finally, energy-dispersive X-ray spectroscopy (EDX) confirmed the chemical composition of the crack surfaces, verifying their LME origin.

3.3. Testing method and setup

This study used the three-point bending test to evaluate the load-bearing capacity of RSW joints. The geometry and dimensions of the component-level test specimens are shown in Fig. 2(a). The test specimen comprised six individual parts: two top hat profiles and two bottom sheets made of DX56D, along with two L-shaped profiles made of DP1200 DH. Initially, the top hat profiles were welded to the L-shaped profiles, with a spacing of 5 mm between them. Subsequently, the assembly was enclosed by the bottom sheets, each attached with four spot welds on the flange.

In a three-point bending scenario, a tensile stress gradient develops along the L-shaped profiles, with the highest tensile stresses occurring at the outermost fibers of the component, particularly near the bottom of the sidewalls. As the bending moment increases toward the center, tensile stress rises correspondingly, placing significant loads on the critical spot welds. This tensile stress distribution heightens the likelihood of crack initiation and propagation in regions with pre-existing defects, such as LME cracks. Consequently, the four spot welds located in the middle of the front and rear sidewalls are subjected to surface tensile stresses. Given the presence of LME cracks, these stresses may accelerate crack growth, potentially leading to spot weld separation or failure due to stress concentration. Therefore, these spot welds represent critical regions where failure is most likely to occur and warrant close observation.

On the other hand, the four spot welds on the bottom sheets primarily function to increase the overall rigidity of the hat profiles, preventing significant deformation in these sections during loading. This design ensures that most of the deformation occurs in the L-shaped profiles. Consequently, while the bottom spot welds contribute to structural stiffness, they are not integral to the failure mechanism of the overall structure. This specific design of the test specimen closely

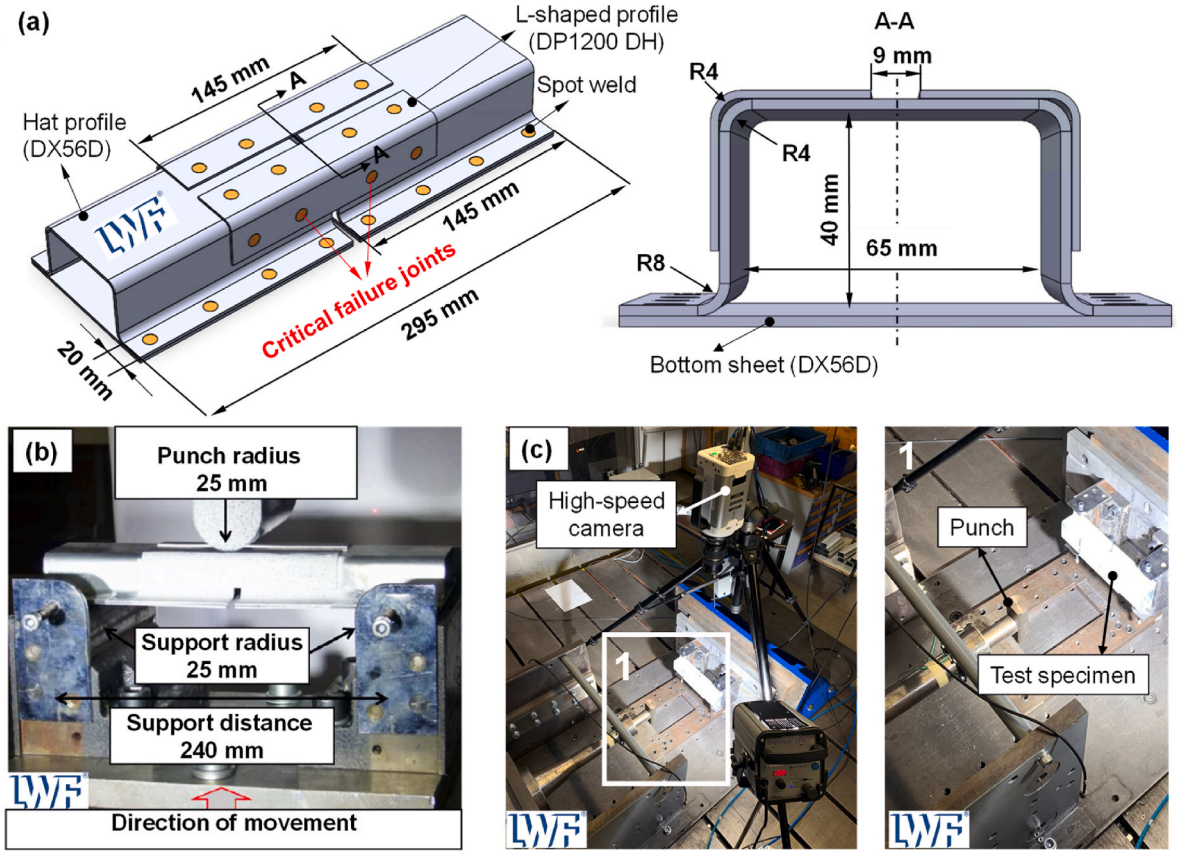

Fig. 2. The designed component geometry(a), the experimental setup for both quasi-static (b) and impact loading (c) conditions.

resembles the shell construction methods commonly employed in real-world components, ensuring that the test setup and conditions closely approximate practical applications. For instance, such structural configurations are widely used in automotive body panels and chassis components. By replicating these conditions, the results obtained from this experimental setup offer deeper insights into the performance of resistance spot-welded structures under real-world loading scenarios, enhancing the applicability of the findings.

The actual experimental setup is shown in Fig. 2(b). As illustrated, the quasi-static tests were conducted using a universal testing machine (Zwick Z100) at a test rate of 10 mm/min. Additionally, digital image correlation (DIC) was employed to measure localized deformation of the L-profile. The measurement system utilized for test specimen's analysis was the 3D GOM Aramis system from Zeiss. Prior to testing, a random speckle pattern was applied to the test object. For optimal contrast, a white primer was first applied, followed by the black speckle pattern. During testing, the cameras recorded the prepared test area and after testing, the GOM Correlate software was later used to calculate the pattern coordinates for each frame, generating comprehensive strain and displacement data.

The impact tests were conducted using a sled test rig under the same clamping conditions. As shown in Fig. 2(c), a high-speed camera from the "Photron Fastcam Nova S series", positioned perpendicular to the observation plane, was used to capture the failure modes of the RSW joints under impact loading. The primary focus of the high-speed camera was to record the crack propagation process, providing detailed insights into how the cracks were initiated and propagated throughout the LME-affected regions of the spot welds. The punch was servo-pneumatically

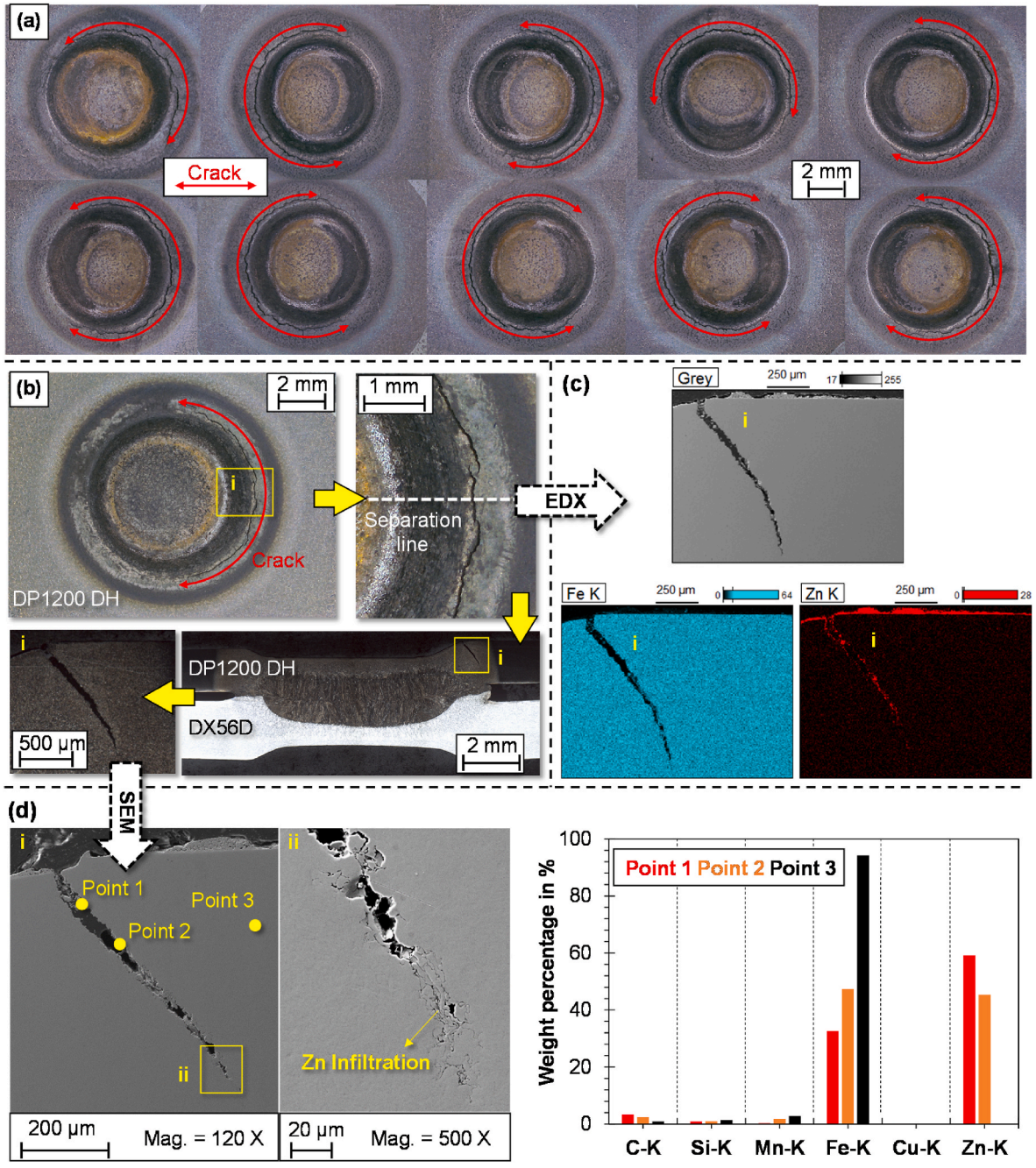

Fig. 3. Crack formation following the welding process (a), metallographic observation for crack characterization (b), EDX analysis confirming the distribution of zinc elements (c), and verification of zinc infiltration (d).

accelerated, and the test was carried out at a test speed of 2 m/s, with supplementary lighting employed to enhance visibility during high-speed video recording.

4. Results and discussion

4.1. Characterization of LME crack formation

The cracks observed in RSW, as shown in Fig. 3(a), were initially characterized using the flat specimen, based on the welding parameters listed in Table 1. These cracks, which occurred after welding, were found on the DP1200 DH side within the HAZ, exhibiting an approximately semicircular shape. To further quantify the crack formation, all specimens were sectioned along the center of the cracks, and metallographic samples were prepared for measurement and characterization. As shown in Fig. 3(b), the analysis revealed that the crack depths ranged from 0.74 mm to 1.07 mm, with an average of 0.87 mm, corresponding to approximately 63.6% of the total sheet thickness. This high percentage indicates significant material degradation in the HAZ, potentially compromising the joint's mechanical integrity. Subsequent SEM and EDX analyses were performed to characterize the cracks further. As depicted in Fig. 3(c), EDX results revealed a substantial accumulation of zinc within the crack sites. This elemental mapping, in conjunction with enrichment data from various points within the crack, as illustrated in Fig. 3(d), confirms the infiltration of liquid zinc into the cracks. The presence of zinc within the cracks conclusively identifies them as LME-induced.

4.2. Influence of LME cracks under quasi-static loading

After identifying and characterizing the LME cracks, subsequent welding experiments were conducted using the same welding parameters on the component-level specimens shown in Fig. 2(a). Thus, it can be considered that the severity of the cracks is comparable to those previously characterized in the flat specimens, as shown in Fig. 3(a). To produce test specimens without LME cracks, which served as the reference group, the nital solution was applied to the planned spot weld positions on the L-shaped profiles (DP1200 DH) to remove the zinc coating. As shown in Fig. 4(a), after testing three specimens, no failure occurred at the joints in the reference group. Instead, failures were observed in the base material (BM) at the gap between the two hat-shaped profiles.

In contrast, test specimens retaining the zinc coating were spot welded to induce LME cracks. Fig. 4(b) illustrates the LME crack morphology before the load-bearing capacity test. In the presented test specimen, the LME crack was located on the upper left side of the spot weld within the HAZ. A comparison of the force-displacement curves between specimens with and without LME cracks, as depicted in Fig. 4(c), reveals distinct differences in behavior. For the reference group (without LME), the load-displacement curves exhibited substantial overlap before failure (marked by the steep drop in the curves). This overlap indicates that failure in these specimens was governed solely by the mechanical properties of the BM. The two distinct drops in the curve correspond to failures in the BM on both sides of the specimen. The reference group achieved an average peak load of 21.02 kN. In contrast, the control group (with LME) displayed marked variability, with the load-displacement curves showing an immediate and pronounced

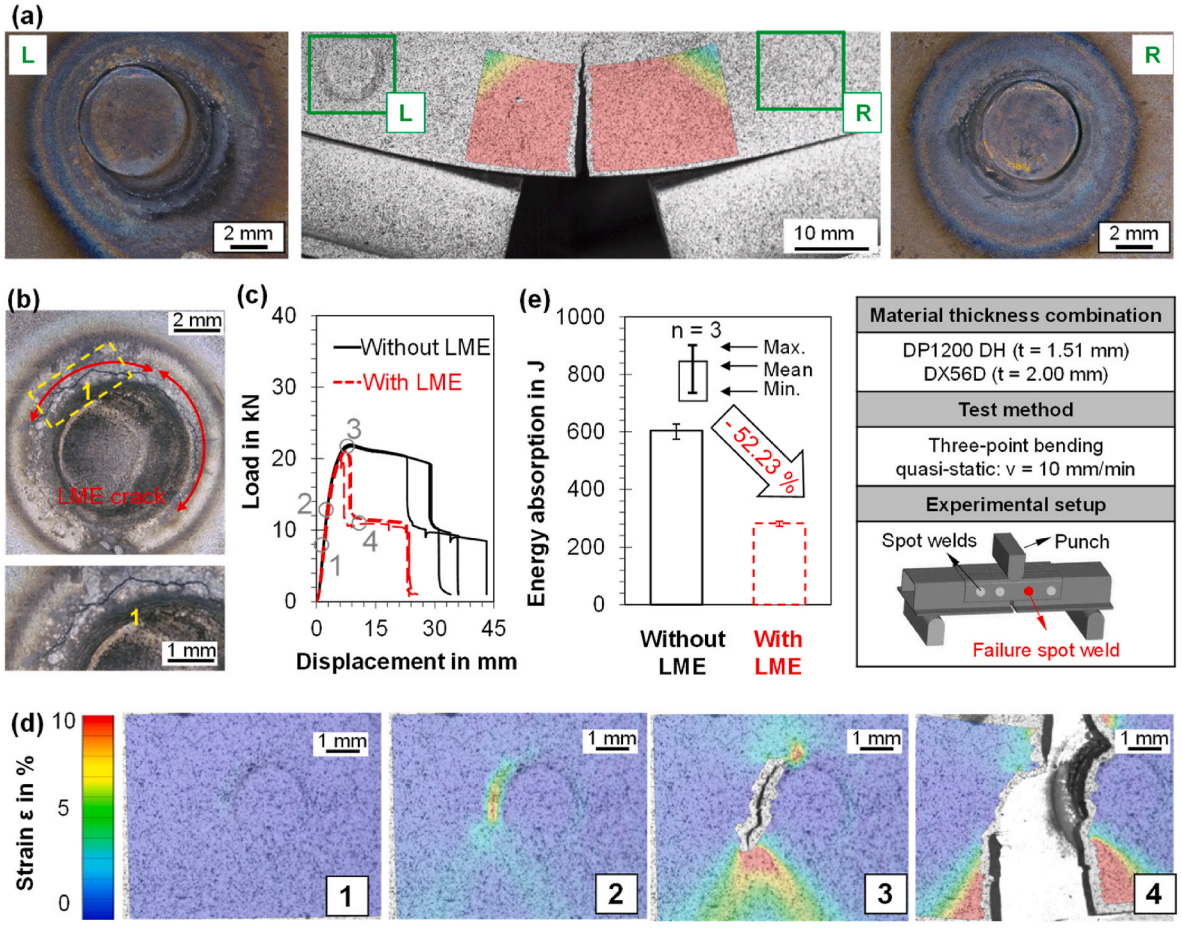

Fig. 4. Failure in the base material (BM) of specimens without LME cracks (a), morphology of LME cracks at the failure point (b), comparison of load-displacement curves with and without LME cracks (c), surface strain distribution during joint failure (d), comparison of energy absorption (e).

decline after reaching peak load. In this group, the average peak load was 20.2 kN, representing a reduction of 0.82 kN (approximately 3.9%) compared to the reference group.

This reduction is attributed to the localized strain behavior near the LME cracks, which was observed during the loading process at various punch displacements, as depicted in Fig. 4(d). In Stages 1 and 2, elevated strain levels were detected in the vicinity of the LME cracks due to stress concentration. Additionally, higher strain levels were also observed in the lower regions near the cracks, attributed to the tensile stress gradient in the three-point bending test, where stress increases with distance from the loading point.

As the load approached its peak, the dominant LME crack propagated downward, driven by stress concentration, causing tearing of the BM and further widening of the crack under tensile stresses. During Stage 4, this crack propagation led to complete joint failure along the pre-existing LME crack, marked by the initial rapid drop in the load-displacement curve. A comparative analysis of energy absorption in specimens with and without LME cracks, as illustrated in Fig. 4(e), revealed that the presence of LME cracks resulted in a 52.23% reduction in energy absorption. This correlation between surface strain and crack propagation offers critical insights into the role of LME cracks in accelerating specimen failure.

4.3. Influence of LME cracks under impact loading

Similar to the quasi-static tests, impact loading tests were first performed on the reference group with the zinc coating removed. As depicted in Fig. 5(a), across three repeated tests at a speed of 2 m/s, the specimens exhibited significant plastic deformation, but no failure in spot welds was observed. This indicates that under impact loading, without the presence of LME cracks, the RSW joints were able to withstand the applied loads without experiencing failure.

For the control group with LME cracks, the force-displacement curves showed a sharp decline after the peak load, as shown in Fig. 5 (b) and (c). In these specimens, the LME crack was located above the spot weld in the HAZ. In contrast to the reference group, where no spot weld failure occurred, the control group exhibited an immediate drop in load capacity after reaching an average peak load of 20.6 kN, which represents a decrease of 2.5 kN (approximately 10.8%) compared to the reference group (average peak load: 23.1 kN).

High-speed camera footage captured the failure process, highlighting the crack propagation across five distinct stages, as shown in Fig. 5(d). During the initial stages (stages 1 and 2), stress concentration at the LME crack site initiated crack growth, propagating from the upper-left to the lower-left of the spot weld. By stage 3, as the load approached its peak, the crack extended below the spot weld, leading to BM tearing due to surface tensile stresses. Ultimately, in stages 4 and 5, the material beneath the spot weld completely tore and the crack propagated upward, resulted in complete spot weld failure. A comparative analysis of energy absorption, as shown in Fig. 5(e), revealed that the presence of LME cracks caused a significant reduction in energy absorption, with specimens showing a 78.25% decrease compared to those without LME cracks. This reduction was significantly higher than the 52.23% reduction observed under quasi-static loading conditions, indicating that the rapid application of kinetic energy during impact loading accelerates the failure process. In conclusion, the results demonstrate that the crack's location and the direction of applied load were critical factors in the failure mechanism. The right side of the crack did not significantly

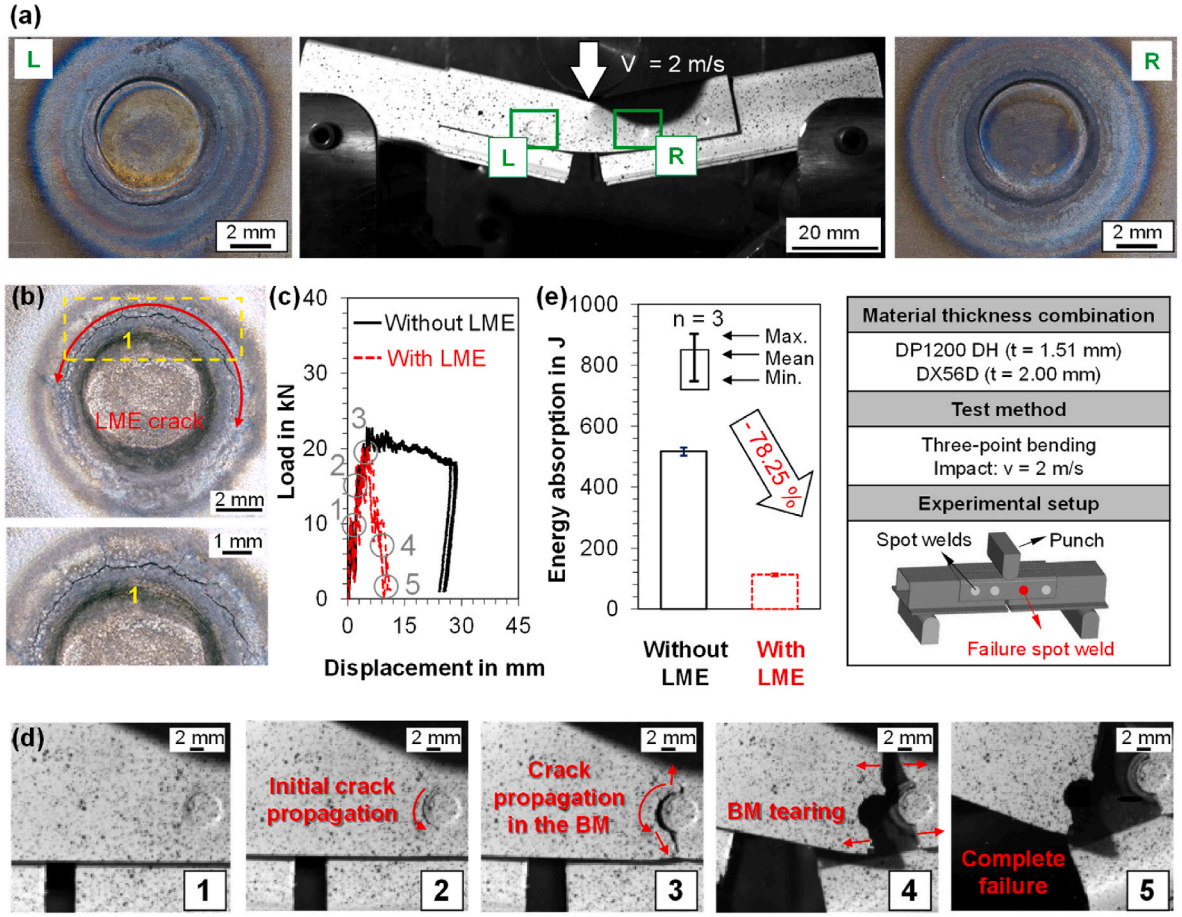

Fig. 5. No failure observed in specimens without LME cracks(a), morphology of LME cracks at the failure point (b), comparison of load-displacement curves with and without LME cracks (c), joint failure process recorded at different stages (d) and comparison of energy absorption (e).

contribute to BM failure, likely due to the concentration of surface tensile stresses on the left side. This emphasizes the importance of considering both crack position and load direction when assessing the impact of LME cracks on joint performance.

5. Conclusion and outlook

In conclusion, this study utilized component-level test specimens to investigate the effects of LME cracks on the mechanical behavior of RSW joints in zinc-coated 3rd generation AHSS under both quasi-static and impact loading. The aim was to provide a component-level specimen configuration that bridges laboratory conditions to component-level applications and addresses the knowledge gap regarding the impact of LME cracks on joint load-bearing capacity under impact loading. This study provides an important reference for understanding the influence of LME cracks on joint performance across various loading conditions at the component level. Based on the results obtained, the following conclusions can be drawn:

- Test specimens without LME cracks exhibited failure in the base material (BM) under both loading conditions, either through fracture or plastic deformation. In contrast, joints with LME cracks failed within the weld region due to stress concentration, leading to crack propagation in the base material and ultimately resulting in complete joint failure, consistent with findings from existing research.
- The study highlighted the critical role of load direction in evaluating the load-bearing capacity of RSW joints with LME cracks. This finding underscores the validity and reliability of the testing methods and specimen dimensions developed in this study, which demonstrated a high degree of repeatability in the results.
- Under the exceptionally high strain rates of impact loading, the influence of LME cracks on the mechanical behavior of joints was found to be more pronounced compared to quasi-static loading. Experimental data revealed that LME cracks in the HAZ, extending beyond 63.6% of the sheet thickness, reduced peak load—by 3.9% under quasi-static loading and by 10.8% under impact loading—and energy absorption—by 52.2% and 78.3%, respectively. This indicates that relying solely on the experimental results under quasi-static loading to evaluate the mechanical behavior of RSW joints with LME cracks is clearly insufficient.
- Under identical experimental boundary conditions during impact loading, specimens without LME cracks experienced no BM failure, showing only plastic deformation. In contrast, specimens with LME cracks failed along the crack path. This observation further underscores the substantial reduction in load-bearing capacity caused by LME cracks under impact loading compared to quasi-static loading.

Given the emphasis of this study on the mechanical behavior of RSW joints influenced by LME, future research should incorporate detailed microstructural characterization of LME cracks and post-failure fracture surfaces. Such analysis would provide essential microscopic-scale insights that further substantiate the conclusions presented here. Moreover, additional investigations are warranted to evaluate a range of material thickness combinations. By utilizing the component-level test specimens developed in this study, future work could systematically assess the effects of LME cracks with varying severity (in terms of depth and length) on joint load-bearing capacity. This approach would enable a more precise determination of tolerable LME crack severity through experimental investigation, contributing to the reliable and safe integration of AHSS in automotive body structures.

CRediT author contribution statement

Keke Yang: Conceptualization, Methodology, Validation, Visualization, Investigation, Formal analysis, Writing – original draft, Writing – review & editing. Matthias Sowada: Investigation, Formal analysis, Validation, Data curation. Viktoria Olfert: Formal analysis, Visualization. Georg Seitz: Visualization, Project administration. Vincent Schreiber: Formal analysis, Project administration. Marcel Heitmann: Investigation, Data curation. David Hein: Conceptualization, Methodology, Formal analysis, Supervision, Writing – review & editing. Max Biegler: Investigation, Data curation, Supervision. Sven Jüttner: Resources, Funding acquisition, Supervision. Michael Rethmeier: Resources, Funding acquisition, Supervision. Gerson Meschut: Resources, Funding acquisition, Supervision. All authors have read and agreed to the published version of the manuscript.

Disclosure statements

No potential conflict of interest was reported by the authors.

Declaration of interests

The authors declare that they have no known competing financial interests or personal relationships that could have appeared to influence the work reported in this paper.

Acknowledgments

The research project " Validation of methods for the avoidance of Liquid Metal Embrittlement on Realistic Principle Components" was funded by the Federal Ministry of Economic Affairs and Climate Action as part of the "Industrial Collective Research" programme on the basis of a resolution of the German Bundestag. This project 21483 BG/P 1488 from the Research Association for steel Application (FOSTA), Düsseldorf, was carried out at Laboratory for material and joining technology (LWF), Paderborn, Institute for material and joining technology (IWF), Magdeburg and Fraunhofer IPK, Berlin.

I acknowledge support for the publication cost by the Open Access Publication Fund of Paderborn University.

References

[1] Meschut G, Matzke M, Hoerhold R, Olfermann T. Hybrid technologies for joining ultra-high-strength boron steels with aluminum alloys for lightweight car body structures. Procedia CIRP 2014;23:19–23. https://doi.org/10.1016/j.procir.2014.10.089.

[2] Ma Y, Shen Y, Hu L, Li Y, Li H. Fracture modeling of resistance spot welded ultra-high-strength steel considering the effect of liquid metal embrittlement crack. Mater Des 2021;210:110075. https://doi.org/10.1016/j.matdes.2021.110075.

[3] Jin W, Lalachan A, Murugan SP, Ji C, Park Y. Effect of process parameters and nugget growth rate on liquid metal embrittlement (LME) cracking in the resistance spot welding of zinc-coated steels. Journal of Welding and Joining 2022;40(6):464–77. https://doi.org/10.5781/JWJ.2022.40.6.2.

[4] Chen S, Zhang Y, Feng Z, editors. Transactions on intelligent welding manufacturing. Singapore: Springer Singapore; 2018.

[5] Nicholas MG, Old CF. Liquid metal embrittlement. J Mater Sci 1979;14(1):1–18. https://doi.org/10.1007/BF01028323.

[6] Mendala J. Liquid metal embrittlement of steel with galvanized coatings. IOP Conf Ser Mater Sci Eng 2012;35:012002. https://doi.org/10.1088/1757-899X/35/1/012002.

[7] Murugan SP, Park Y, Vijayan V, Ji C. Four types of LME cracks in resistance spot welding of Zn-coated advanced high-strength steels. Weld J 2020;99(3):75s–92s. https://doi.org/10.29391/2020.99.008.

[8] Böhne C, Meschut G, Biegler M, Frei J, Rethmeier M. Prevention of liquid metal embrittlement cracks in resistance spot welds by adaption of electrode geometry. Sci Technol Weld Join 2020;25(4):303–10. https://doi.org/10.1080/13621718.2019.1693731.

[9] Böhne C, Meschut G, Biegler M, Rethmeier M. Avoidance of liquid metal embrittlement during resistance spot welding by heat input dependent hold time adaption. Sci Technol Weld Join 2020;25(7):617–24. https://doi.org/10.1080/13621718.2020.1795585.

[10] Fernandes PJL, Jones DRH. Mechanisms of liquid metal induced embrittlement. Int Mater Rev 1997;42(6):251–61. https://doi.org/10.1179/imr.1997.42.6.251.

[11] Vermeersch M, de Waele W, van Caenegem N. LME susceptibility of galvanised welded structures of high strength steels. International Journal of Sustainable Materials Engineering and Design 2011;2(3):442–7. https://doi.org/10.21825/scad.v2i3.20543.

[12] Beal C, Kleber X, Fabregue D, Bouzekri M. Liquid zinc embrittlement of twinning-induced plasticity steel. Scripta Mater 2012;66(12):1030–3. https://doi.org/10.1016/j.scriptamat.2011.12.040.
[13] Ludwig W, Pereiro-López E, Bellet D. In situ investigation of liquid Ga penetration in Al bicrystal grain boundaries: grain boundary wetting or liquid metal embrittlement? Acta Mater 2005;53(1):151–62. https://doi.org/10.1016/j.actamat.2004.09.012.
[14] Bhattacharya D. Liquid metal embrittlement during resistance spot welding of Zn-coated high-strength steels. Mater Sci Technol 2018;34(15):1809–29. https://doi.org/10.1080/02670836.2018.1461595.
[15] Siar O, Dancette S, Dupuy T, Fabrègue D. Impact of liquid metal embrittlement inner cracks on the mechanical behavior of 3rd generation advanced high strength steel spot welds. J Mater Res Technol 2021;15:6678–89. https://doi.org/10.1016/j.jmrt.2021.11.100.
[16] Gaul H, Weber G, Rethmeier M. Influence of HAZ cracks on fatigue resistance of resistance spot welded joints made of advanced high strength steels. Sci Technol Weld Join 2011;16(5):440–5. https://doi.org/10.1179/1362171810Y.0000000031.
[17] Benlatreche Y, Duchet M, Dupuy T, Cornette D, Carollo G. No effect of liquid metal embrittlement cracks on the mechanical performances of spot welds. In: 5th international conference on steels in cars and trucks, Amsterdam (Netherlands); 2017. p. 18–22. June.
[18] Choi D, Uhm S, Enloe C, Lee H, Kim G. Liquid metal embrittlement of resistance spot welded 1180TRIP steel – effects of crack geometry on weld mechanical performance. In: Contributed papers from MS&T17;; 2017. p. 454–62.
[19] DiGiovanni C, Biro E, Zhou NY. Impact of liquid metal embrittlement cracks on resistance spot weld static strength. Sci Technol Weld Join 2019;24(3):218–24. https://doi.org/10.1080/13621718.2018.1518363.
[20] DiGiovanni C, Han X, Powell A, Biro E, Zhou NY. Experimental and numerical analysis of liquid metal embrittlement crack location. J Mater Eng Perform 2019;28(4):2045–52. https://doi.org/10.1007/s11665-019-04005-2.
[21] Sønstabø JK, Morin D, Langseth M. Static and dynamic testing and modelling of aluminium joints with flow-drill screw connections. Int J Impact Eng 2018;115:58–75. https://doi.org/10.1016/j.ijimpeng.2018.01.008.
[22] Biro E. Effect of LME cracking on RSW strength: the remaining question to integrate LME susceptible materials into the body-in-white. In: Commission III – IIW annual assembly 2023; 2023.
[23] DIN EN ISO 18278-2:2016-09, WiderstandsschweißenSchweißeignungTeilVerfahren zum Bewerten der Eignung für das Widerstandspunktschweißen (ISO-Deutsche Fassung EN ISO 18278-2:2016).
[24] DIN EN ISO 5821:2010-04, widerstandsschweißen-punktschweiß-elektrodenkappen (ISO-deutsche fassung EN ISO 5821:2009).
[25] SEP1220-2:2011. Testing and documentation guideline for the joinability of thin sheet of steel – part 2: resistance spot welding. 2011.
[26] Siar O, Benlatreche Y, Dupuy T, Dancette S, Fabrègue D. Effect of severe welding conditions on liquid metal embrittlement of a 3rd-generation advanced high-strength steel. Metals 2020;10(9):1166. https://doi.org/10.3390/met10091166.
[27] Böhne C, Meschut G, Biegler MA, Rethmeier M. The influence of electrode indentation rate on LME formation during RSW. Weld J 2022;101(7):197–207. https://doi.org/10.29391/2022.101.015.
[28] VDA 239-100. Sheet steel for cold forming. Berlin, Germany: Verband der Automobilindustrie e.V. (VDA); 2016.
[29] Patel M, Shojaee M, Sherepenko O, Midawi A, Ghassemi-Armaki H, Biro E. Mitigating the influence of industrially relevant disturbances on LME severity of dissimilar resistance spot welded advanced high-strength steels. J Mater Res Technol 2023;26:22–31. https://doi.org/10.1016/j.jmrt.2023.07.176.